



FluidUrban v1.0: Enhancing Urban Ventilation and Pollutant Dispersion Modelling with Three-dimensional Dynamic Adaptive Meshes Optimisation

5 Xiaofei Wu¹, Siyang Chen¹, Jinxi Li², Yu Zhang¹, Zifa Wang², Pu Gan¹, Jie Zheng³, Fangxin Fang³

¹Climate Change and Resource Utilization in Complex Terrain Regions Key Laboratory of Sichuan Province, Chengdu Plain Urban Meteorology and Environment Observation and Research Station of Sichuan Province, School of Atmospheric Sciences, Chengdu University of Information Technology, Chengdu, 610225, China

10 ²State Key Laboratory of Atmospheric Environment and Extreme Meteorology, Institute of Atmospheric Physics, Chinese Academy of Sciences, Beijing, 100029, China

³Applied Modelling and Computation Group, Department of Earth Science and Engineering, Imperial College London, London, SW7 2AZ, United Kingdom

Correspondence to: Xiaofei Wu (wuxf@cuit.edu.cn)

15

Abstract. Simulating urban airflow and pollutant dispersion requires resolving multiscale physical processes, from large-scale meteorological forcing to highly localized building-induced turbulence. To accurately capture these multiscale urban flow fields, this study introduces FluidUrban v1.0, an advanced modelling system built upon the Fluidity solver and centred on a three-dimensional Dynamic Adaptive Mesh Optimization (DAMO) framework. By dynamically adapting mesh resolution in response to the evolution of flow physics and scalar gradients, DAMO concentrates computational resources on critical high-gradient regions such as building wakes, shear layers and scalar sharp plume. The model's performance is systematically evaluated against high-fidelity “WOTAN” wind-tunnel experimental data under varying surface roughness conditions and inflow directions. The results demonstrate that the FluidUrban with DAMO framework consistently outperforms traditional non-uniform fixed meshes (FIXM) by accurately capturing complex urban wind fields and pollutant concentration. For normalized wind speed, FluidUrban with DAMO achieved a Mean Absolute Error (MAE) of 0.187, representing a notable reduction from the 0.214 simulated by FIXM. In terms of wind direction, the model reduced the MAE by up to 38.4% in medium roughness and 36.1% in high roughness conditions, respectively, during realistic oblique inflow scenarios. Furthermore, for pollutant dispersion, the model effectively suppresses numerical diffusion and maintained sharply plume gradients, achieving an 89% compliance rate with established atmospheric model evaluation standards (FB, NMSE, and MG), compared to only 50% for FIXM. While DAMO introduces runtime cost for mesh regeneration, this cost is strategically offset by the optimization of the accuracy-efficiency balance. Following the systematic evaluation, FluidUrban v1.0 was applied to a realistic urban scenario, demonstrating its robust capability to resolve the complex flow fields and spatial heterogeneity within real urban morphologies. Thus, FluidUrban v1.0 demonstrates to be a robust

20

25

30



35 aerodynamic tool for resolving the transient, small-scale flow structures critical to pollutant transport, establishing a solid
foundation for the future integration of comprehensive urban physical components, including radiation, vegetation, and full
energy-balance physics.

1 Introduction

40 Projections indicate that by 2050, over 70% of the global population will reside in cities, with the growth of megacities
expected to accelerate in the coming decades (United Nations, 2019). This rapid urbanization threatens to exceed urban
carrying capacities, presenting substantial environmental, infrastructural, and social challenges. Among these, urban heat
island and air pollution have become critical concerns with significant implications for human health and sustainable
development (Connerton et al., 2020; Khomenko et al., 2021; Apte and Manchanda, 2024). The efficacy of urban heat and
45 pollutant dispersion is directly linked to urban ventilation, which is shaped by the complex interaction between building
morphology, city density, and local aerodynamic conditions (da Silva et al., 2021, Liang and Zheng, 2026). Accurately and
quickly modelling these wind fields is therefore vital for designing sustainable residential environments and effective emission
control strategies. However, capturing the multiscale nature of pollutant transport, driven by heterogeneous surface heating
and complex urban geometries, requires high-resolution, physically consistent numerical simulations (Zhang et al., 2018;
50 Nagai et al., 2021; Khan et al., 2025). As a result, advanced numerical modelling has emerged as an essential tool for evaluating
ventilation potential and guiding urban atmospheric management (Badach et al., 2020; Khan et al., 2021; Liu et al., 2023).
55 With the rapid development of the computer hardware, Computational Fluid Dynamics (CFD) simulations are becoming an
efficient and important method to conduct the study of urban wind fields and air pollutant dispersion (Hang et al., 2013; Mottet
et al., 2020; Zhong et al., 2022; Kusaka et al., 2024), which output detailed information of 3D flow variables in the whole
computational field and display them visually. However, modeling airflow and pollutant dispersion in urban areas is
complicated by the tight coupling of multiscale physical processes (Di Sabatino et al., 2013). Large-scale meteorological
60 forcing determines the prevailing wind, whereas small-scale interactions with building geometries induce complex vortex
shedding and turbulence, which can significantly modifying the mean flow field (Giani and Crippa, 2024). This creates an
extra wide spatial spectrum to resolve: spanning from the planetary boundary layer that transports plumes over long distances,
down to the inertial sub-range turbulence within street canyons that governs pedestrian-level exposure. Chemical aging of
pollutants further complicates this, as emissions undergo rapid transformation immediately upon release from localized sources
65 (e.g., smokestacks or roadways) before dispersing over the urban canopy (Weger and Heinold, 2023). Simulating a large city
with a fixed grid fine enough to resolve individual building features is computationally infeasible. These methods often struggle
to capture highly localised and transient dynamic processes, such as building-induced vortices and shear layers, as well as flow
variations around building edges and within street canyons (Jackson et al., 2015; Pesci et al., 2018). To address this,
conventional CFD approaches utilize nested or stretched meshes to statically refine specific regions of the domain (Park and
Kim, 2024). However, such methods suffer from critical shortcomings: they impose nested boundaries that create artificial



wave reflections at grid interfaces, introduce significant numerical diffusion as plumes drift into coarser zones, and waste computational resources by over-refining inactive regions where high resolution is unnecessary. Consequently, Three-Dimensional (3D) Dynamic Adaptive Mesh Optimization (DAMO), often implemented via Adaptive Mesh Refinement (AMR), offers the most viable path forward. By dynamically refining grid resolution in real-time response to flow physics (such as velocity) and scalar gradients (such as pollutant concentration), DAMO enables a unified modeling system (AMCG, 2014). This approach seamlessly couples scales, accurately capturing the non-linear feedback loops between regional meteorological forcing and local street-canyon turbulence without the computational cost of uniformly fine grids. By automatically refining and coarsening the mesh in response to solution features such as velocity gradients or vorticity, DAMO enables computational resources to be focused where they are most needed (Zheng et al., 2015; Sezen and Atlar, 2022; Yu et al., 2024). This technique has shown considerable potential for improving both accuracy and computational efficiency across a range of geophysical fluid applications, including boundary-layer dynamics (Bauer et al., 2020), cloud–aerosol interaction processes (Han et al., 2023), and atmospheric chemical transport mechanisms (Yang et al., 2025).

Despite DAMO has demonstrated its potential to capture building wake dynamics and high-gradient pollutant structures (Zheng et al., 2021; Wu et al., 2023; Li et al., 2025), a critical need remains to transition generic adaptive solvers to dedicated urban multi-physics frameworks. To address this, this study introduces FluidUrban v1.0, a novel urban modeling framework centered on 3D DAMO. FluidUrban v1.0 is built upon the well-established open-source Fluidity solver (Imperial College London), which has proven robust in large-scale atmospheric advection and complex terrain simulations utilizing anisotropic adaptive unstructured meshes (Pain et al., 2005; Li et al., 2018). Building upon this mathematical foundation, FluidUrban v1.0 is specifically developed to adapt these advanced numerical techniques for high-resolution urban micrometeorology. By developing a dedicated 3D urban geometry and unstructured mesh generator, and coupling it with urban boundary conditions, the model serves as a foundational framework capable of resolving highly localized and transient dynamic processes, such as building-induced vortices and shear layers, that are often smoothed out by traditional approaches (Jackson et al., 2015; Pesci et al., 2018).

Concurrently, establishing the reliability of this newly developed framework requires systematic and quantitative evaluation. Much of the existing studies of DAMO simulation focus on qualitative visual improvements, leaving a critical gap in quantifying the specific gains in accuracy and computational efficiency that DAMO offers relative to fixed-mesh benchmarks (Zheng et al., 2015; Tarraf et al., 2024). To address these validation gaps, wind tunnel experiments (WTE) usually serve as the “ground truth” standard for benchmarking urban CFD models. Unlike field measurements, which are limited by uncontrollable meteorological variability and sparse sampling, WTE provides high-fidelity and controllable datasets ideal for isolating specific flow phenomena like cavity recirculation and street-canyon ventilation. While established databases like CEDVAL (Hamburg University) and the Architectural Institute of Japan (AIJ) guidelines remain the foundation for verifying mean flow and turbulence statistics (Tominaga et al., 2008; Ricci et al., 2017), recent work by Wang et al. (2025) demonstrates that validating adaptive models requires not just point-measurements, but dense and spatially-resolved data to capture the sharp gradients of pollutant plumes in the inertial sub-range. Furthermore, contemporary studies utilise these datasets to assess solver



100 fidelity under complex transient conditions, such as gusty cross-canyon flows, which are often smoothed out by traditional
RANS approaches but are critical for accurate exposure modelling (Gromke, 2011; Cui et al., 2016; Arafa and Zinat, 2025).
Thus, the primary objective of this study is to develop a novel urban modeling framework FluidUrban v1.0 centered on 3D
DAMO and provide a comprehensive validation of the model against wind-tunnel experiments and standard fixed-mesh
105 simulations, thereby quantifying the benefits of 3D adaptivity for urban flow and pollutant dispersion. The remainder of the
paper is organised as follows: Section 2 details the model setup, focusing on the model development, the governing equations
and implementation of the physics-driven DAMO algorithm. Section 3 presents a quantitative performance evaluation for both
urban wind flows and pollutant dispersion, and analyses how the adaptive strategy captures key urban flow features. Section
4 show the performances of the model used in a realistic urban scenario simulation. Finally, Section 5 summarises the principal
conclusions and discusses its implications of this framework for next generation of urban environmental modelling.

110 **2 Methodology**

2.1 Model development

FluidUrban v1.0 is built upon the open-source Fluidity solver. The core advancement of this new framework lies in the
development of a dedicated generator of 3D urban geometry and unstructured meshes, which is subsequently coupled with
urban-specific micrometeorological boundary conditions. This systematic integration enables the model to accurately initialize
115 and dynamically resolve complex urban flow topologies.

2.1.1 Urban geometry and unstructured mesh generator

While DAMO optimises the meshes during runtime, generating an accurate geometry and initial mesh is a prerequisite to
explicitly resolve the complex morphology and heterogeneous geometry of the realistic urban canopy. To achieve this, a
dedicated 3D urban geometry and unstructured mesh generator was developed, utilising the computational geometry engine
120 of GMSH. GMSH is a robust 3D finite element mesh generator featuring a built-in CAD engine, designed to facilitate
parametric input and advanced spatial visualization (<https://gmsh.info/>). The mesh generation workflow for FluidUrban
executes through three automated steps:

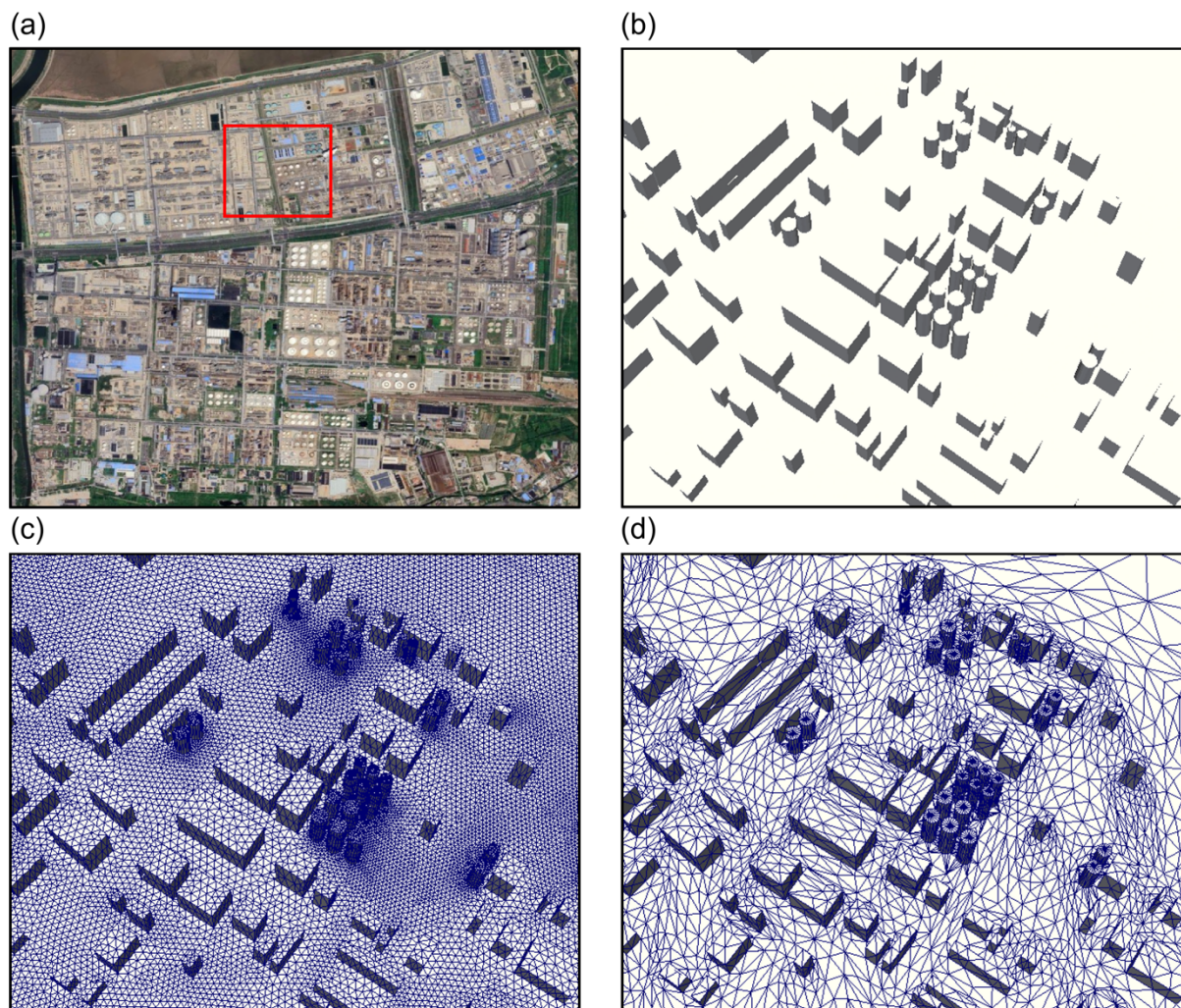
(1) Data Acquisition and Outline Extraction: 2D building polygons and height datasets are primarily sourced from public
geodatabases, such as OpenStreetMap (OSM). For simulation domains lacking comprehensive 3D building information data,
125 the framework includes a custom utility designed to extract building polygons directly from high-resolution satellite imagery
utilizing a supervised Support Vector Machine (SVM) classification algorithm.

(2) 3D Geometry Reconstruction and Domain Setup: Using the extracted building polygons and heights, a custom Python
script processes the datasets to reconstruct the 3D urban morphology. These routine outputs a native GMSH geometry file
(.geo), explicitly defining the topological hierarchy of points, lines, land and building surfaces, and the computational domain
130 that represent the physical 3D urban canopy (**Figure 1b**). During the subsequent simulation, these structural components and



domain boundaries act as fixed constraints. The dynamic mesh adaptation process alters only the internal fluid grid without changing the spatial coordinates of the defined topology.

(3) Initial Mesh Generation and Adaptive Optimization: An initial 3D unstructured mesh is subsequently generated from the .geo geometry file using the GMSH software (Figure 1c). While the underlying geometry provides the fixed structural baseline, this static mesh serves strictly as the initial computational grid for FluidUrban. Upon simulation initialisation, the solver's DAMO algorithm dynamical refine and coarse the local mesh elements in real-time response to evolving flow physics, such as localised wind shear or pollutant dispersion gradients (Figure 1d).



140 **Figure 1: Workflow of 3D urban geometry reconstruction and adaptive mesh generation: (a) high-resolution satellite imagery of the study area and a zoom-in view of (b) the reconstructed 3D urban geometry, (c) the initial unstructured mesh and (d) the adaptive**



mesh generated with DAMO during simulation. In (a), the satellite imagery is derived from © Google Earth (<https://earth.google.com/web/>).

2.1.2 Urban turbulence inlet boundary conditions

145 Accurately prescribing inflow conditions is critical for reproducing the realistic aerodynamic behaviour of the atmospheric boundary layer as it interacts with the urban canopy. To achieve this, FluidUrban implements a turbulent inlet velocity profile driven by a synthetic eddy method (SEM). This approach superimposes realistic and transient turbulent fluctuations over a theoretical mean wind profile. The time-averaged streamwise velocity $\bar{u}(z)$, is prescribed assuming a neutral atmospheric boundary layer (ABL) following the standard Log-Law profile or Power-Law Profile. To explicitly resolve the transient, 150 energy-containing scales of turbulence entering the domain, the instantaneous velocity vector $u_i(x, t)$ at the inlet is computed as the sum of the mean flow and the instantaneous velocity fluctuations:

$$u_i(\mathbf{x}, t) = \bar{u}_i(\mathbf{x}) + u'_i(\mathbf{x}, t) \quad (1)$$

Following the SEM framework, the turbulent fluctuations, $u'_i(x, t)$ are generated by injecting a distinct number of synthetic eddies (N) and that convect through the inlet plane. The spatial and temporal distribution of these fluctuations is mathematically 155 formulated as:

$$u'_i(x, t) = \sum_{k=1}^N a_{ij} \varepsilon_j^k f_\sigma(\mathbf{x} - \mathbf{x}^k(t)) \quad (2)$$

Where a_{ij} represents the Cholesky decomposition of the prescribed local Reynolds stress tensor (R_{ij}), which scales the intensity of the fluctuations. For each k-th eddy, ε_j^k is a random sign distribution (typically) to ensure zero mean perturbation, f_σ is a normalized spatial shape function defining the coherent structure and characteristic length scale of the eddy, and $\mathbf{x}^k(t)$ 160 denotes the instantaneous position of the eddy center. The comprehensive mathematical derivation, including the specific geometric shape functions and the spatial-temporal numerical implementation of this SEM upon unstructured meshes within the Fluidity architecture, is detailed extensively by Pavlidis et al. (2010).

2.2 Model equations

The FluidUrban integrates the 3D incompressible Navier–Stokes equations coupled with an advection–diffusion equation for 165 scalar transport. To represent turbulence in the urban boundary layer, the model employs a large-eddy simulation (LES) framework. LES explicitly resolves energy-containing turbulent eddies while parameterising subgrid-scale (SGS) motions, thereby balancing numerical accuracy and computational cost. The filtered, compressible Navier–Stokes equations under the Boussinesq approximation are employed for wind-field simulations:

$$\nabla \cdot \mathbf{u} = 0 \quad (3)$$

$$170 \frac{\partial(\rho U)}{\partial t} + \nabla \cdot (\rho \mathbf{U} \mathbf{U}) = -\nabla p + \nabla \cdot (\mu \nabla \mathbf{U}) + \rho \mathbf{g} \quad (4)$$



where ρ is the fluid density, \mathbf{U} the velocity vector, p the pressure, μ the dynamic viscosity, and \mathbf{g} the gravitational acceleration. For pollutant dispersion, the model employs the scalar advection-diffusion equation:

$$\frac{\partial c}{\partial t} + \nabla \cdot (\mathbf{u}c) = \nabla \cdot (\bar{\kappa} \nabla c) - \sigma c + F \quad (5)$$

where c is the pollutant mass concentration, $\mathbf{u} = (u, v, w)^T$ is the velocity vector, $\bar{\kappa}$ is the diffusion coefficient tensor, σ is the absorption coefficient (the term $-\sigma c$ is sometimes referred to as Rayleigh or linear damping), and F denotes source or reaction terms. In most environmental flow simulations, diffusion is assumed isotropic, so $\bar{\kappa}$ can be simplified as $\bar{\kappa} = D_{AB} \cdot I$, with D_{AB} denoting the binary molecular diffusion coefficient given by the Fuller et al. (1966) correlation:

$$D_{AB} = \frac{CT^b \left(\frac{1}{M_A} + \frac{1}{M_B} \right)^{1/2}}{p \left[(\sum_A v_{i,A})^{1/3} + (\sum_B v_{i,B})^{1/3} \right]^2} \quad (6)$$

In this equation, C is a constant fitting experimental data to ensure consistency between simulation results and measurements. T denotes the absolute temperature, p represents the ambient pressure, and b is the temperature-dependence exponent. In this study, $b = 1.75$ is the temperature-dependent exponent, covering a wide range of binary gas systems. M_A and M_B denote the molecular weights of the two species, with the lighter species generally exhibiting higher diffusivity, and $v_{i,A}$ and $v_{i,B}$ are the molecular diffusion volumes of each gas component.

The pollutant mixture considered here comprises carbon dioxide (CO_2 , $M_A = 44 \text{ g mol}^{-1}$) and butane (C_4H_{10} , $M_B = 58 \text{ g mol}^{-1}$), with a mean density $\rho_g \approx 1.8411 \text{ kg m}^{-3}$ at standard conditions. The effective diffusion coefficient is obtained via a weighted average of the components, accurately reflecting mixture effects on transport (Nonaka, 2025).

2.3 WTE datasets

The performance of the FluidUrban v1.0 is evaluated using the WOTAN WTE dataset provided by the Environmental Wind Tunnel Laboratory (EWTL) at the University of Hamburg, Germany (Michel, 2023). This wind tunnel features a large test section with dimensions of 18 m in length, 4 m in width and 3 m in height. An idealised industrial-area model, geometrically scaled at 1:100 and representing a $300 \text{ m} \times 300 \text{ m}$ real-world site, was employed to study flow and pollutant dispersion in a typical factory layout (**Figure 2**). The model geometry was derived from aerial imagery and building data of an actual industrial park, ensuring a realistic representation of obstacle arrays and pollutant release scenarios.

The WOTAN WTE reproduce two atmospheric boundary-layer stability regimes, including medium roughness (MR) and high roughness (HR), corresponding to the surface characteristics of suburban open terrain and dense urban areas, respectively. These regimes are achieved by combining upstream turbulence generators with surface roughness elements. Following the VDI 3783/12 guidelines for physical modelling of the ABL (VDI, 2000), key flow parameters, including vertical wind speed profiles, turbulence intensity, turbulence energy spectra, and lateral uniformity, are measured and validated to ensure dynamical similarity between the wind-tunnel flow and the real atmosphere.



Figure 2: Idealized industrial park model inside the WOTAN wind tunnel. View from the rear of the wind tunnel looking toward the model along the x-axis. (form Michel, 2023)

2.4 Simulation configurations

2.4.1 Domain and boundary conditions

The validity of the comparison relies on the principles of physical similarity and Reynolds number independence, all simulations are performed at full scale, with the computational geometry replicating the wind-tunnel model. The computational domain precisely replicates the geometry of the wind-tunnel model (**Figure 3**), representing an idealised medium density urban block. The layout comprises twenty rectangular buildings with varying shapes, each 15 m in height. The central building, measuring 60 m in length, 30 m in width and 15 m in height, contains two pollutant release openings (S1 and S2) on opposing side walls, each with an area of 16 m².

Following the COST Action 732 best-practice guidelines for computational wind engineering (Franke et al., 2011), the numerical domain is extended in the horizontal and vertical directions to minimize boundary influence on the internal flow field, yielding total dimensions of 1200 m × 1200 m × 150 m. A neutral ABL flow is prescribed via the boundary conditions. At the inlet, a power-law wind profile is applied to match the wind tunnel conditions for MR ($z_0 = 0.06$ m, $\beta = 0.17$) and HR ($z_0 = 0.29$ m, $\beta = 0.23$), as illustrated in **Figure 4**. The outlet is set as a pressure boundary, permitting free development of the flow. Lateral and upper boundaries are specified as symmetrical planes with slip conditions, imposing zero normal velocity, while all ground and building surfaces are treated as no-slip walls. Consistent with the wind-tunnel campaign, three wind directions are simulated: a 0° inflow case (M1), a 90° case (M2), and a 30° tilted case (M3). For pollutant dispersion simulations, the main building acts as the emission source, with the two openings (S1 and S2) releasing pollutants at a constant rate (**Figure 3**). The complete set of simulation configurations is summarised in **Table 1**.

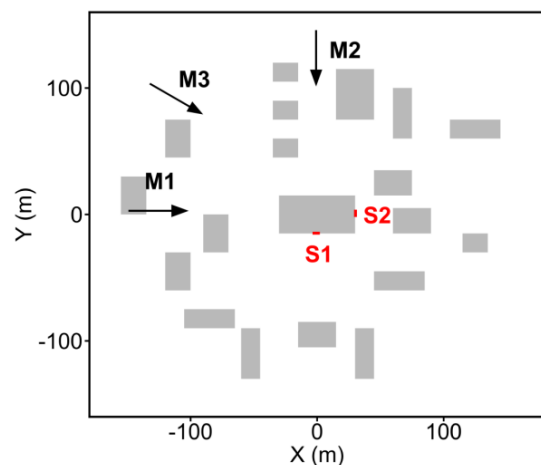


Figure 3: Plan view of the idealized industrial park layout. Gray areas indicate buildings, S1 and S2 mark the two emission sources on the central building. Arrows indicate the three different inlet wind directions (M1: 0°, M2: 90°, M3: 30°).

225

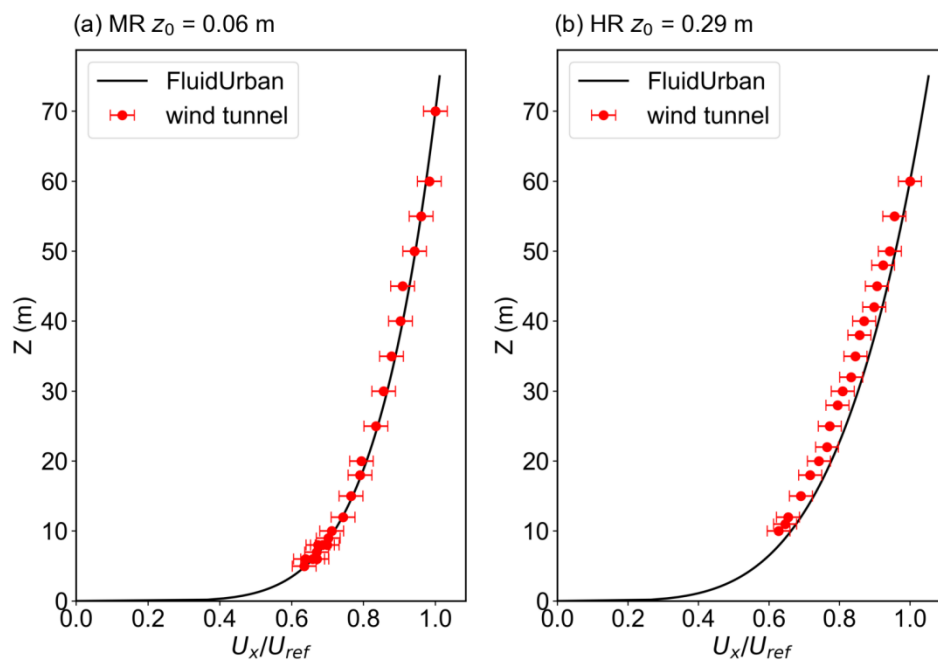


Figure 4: Mean profiles of the inlet flow for the wind-tunnel experiment (red symbols) and the FluidUrban simulation (black solid lines), error bars indicate the standard deviation. (a) the medium roughness boundary condition ($z_0 = 0.06$ m) and (b) the high roughness boundary condition ($z_0 = 0.29$ m).

230



Table 1. Key parameter settings for numerical simulation cases of the idealized industrial park. Case denotes the experimental case identification name. BL represents the boundary condition, expressed by the roughness height (z_0). Inlet Flow indicates the wind direction of the inlet boundary, and Source refers to the emission source identification number used in the simulation.

Case	BL	Inlet Flow	Source
MR-M1-S2	$z_0 = 0.06$ m	0°	S2
MR-M2-S1	$z_0 = 0.06$ m	90°	S1
MR-M3-S1	$z_0 = 0.06$ m	30°	S1
HR-M1-S2	$z_0 = 0.29$ m	0°	S2
HR-M2-S1	$z_0 = 0.29$ m	90°	S1
HR-M3-S1	$z_0 = 0.29$ m	30°	S1

235 2.4.2 Mesh adaptivity setting

A notable feature of the FluidUrban model is its advanced anisotropic dynamic mesh adaptivity functionality, which enables efficient capture of multi-scale physical processes through continuous optimisation of mesh distribution (Zheng et al., 2015; Zheng et al., 2021; Wu et al., 2023). The core of this technique is an anisotropic mesh adaptivity method based on the Hessian matrix, which aims to dynamically allocate computational resources to regions where they are most needed, while adhering to user-defined accuracy constraints. For the wind field and pollutant dispersion simulations in this study, the adaptive workflow proceeds as follows:

(1) The three velocity components u , v , and w are selected as primary target fields for adaptivity. At each adaptation step, the solver computes the Hessian of each field on the current mesh to quantify spatial curvature. Regions of high gradient and strong curvature, such as shear layers and concentration fronts, are assigned finer resolution and more mesh elements.

(2) Based on user-prescribed interpolation error bounds ϵ and the corresponding Hessian matrices, a separate metric tensor M is generated for each target variable. Considering the physical characteristics of urban wind fields, a relatively loose error bound is prescribed for the streamwise wind speed u ($\epsilon_u = 0.5$ m s⁻¹), whereas stricter bounds are applied to the vertical and lateral components ($\epsilon_v = \epsilon_w = 0.15$ m s⁻¹), which better capture building-induced flow separation and small-scale vortices. These individual metric tensors are combined via matrix transformation ($M = M_u \cap M_v \cap M_w \cap M_c$) to form a unified metric tensor, ensuring that the accuracy requirements of all physical fields are met simultaneously.

(3) The composite metric tensor is smoothed to suppress abrupt local variations in the cell size that could lead to numerical instability. A global scaling is then applied to limit the total number of mesh nodes to a predefined target (2.0×10^5 in this study), ensuring computational efficiency.



255

(4) The optimised metric tensor is passed to the mesh generator, which employs the h-adaptation method (Pain et al., 2005) to produce a new anisotropic unstructured mesh. Field variables from the original mesh are interpolated onto the new mesh via a Galerkin projection algorithm (Farrell et al., 2009; Savre et al., 2016), completing one adaptive iteration.

260

In the evaluation simulations, the time step is set to 1 s, and DAMO is performed every 20 time steps, based on the posterior error of the wind field. The initial mesh resolution is 5 m in building-surface regions and 20 m elsewhere. As the simulation progresses, regions with strong gradients are refined to 2 m, while regions with weak gradients remain at or are coarsened to 20 m.

265

For comparison, a control case was established using a non-uniform fixed mesh (FIXM) generated via GMSH. To capture near-wall gradients while maintaining computational efficiency, the mesh resolution is refined to 2 m around the building surfaces and is configured to expand to 20 m at the top of the domain. This mesh configuration remains constant throughout the simulation. To isolate the impact of the mesh adaptivity, all physical parameterizations and boundary conditions in the control case (FIXM) are kept identical to those employed in the adaptive configuration. Consequently, the discretization strategy remains the sole varying factor between the two simulations, ensuring that simulated differences in the flow field and air pollutant are attributable exclusively to the mesh resolution and the dynamic refinement process. In this study, mesh resolution is defined in terms of the equivalent resolution, computed as a shape-weighted average across the domain (Müller et al., 2013). Specifically, the area of each triangular element is converted to the side length of an equilateral triangle of equal area, taken as its equivalent edge length. The global equivalent resolution is then obtained by an area-weighted average of these lengths, providing a consistent basis for comparing simulation errors and computational efficiency between DAMO and FIXM.

270

275

The FluidUrban simulations require a spin-up period to reach a statistically steady state. Because the six experiments do not reach this state simultaneously, a consistent comparison is ensured by analysing the final 1400 seconds of data ($t = 600$ s to $t = 2000$ s), using the experiment with the latest onset of steady state as the reference point.

2.5 Evolution metrics

The quantitative evaluation of the urban wind field simulation is first based on the Mean Error (ME) of the horizontal resultant wind speed $|\bar{U}|$ is calculated as:

$$ME = \frac{1}{n} \sum_{i=1}^n (|U_i^M| - |U_i^O|) \quad (7)$$

280

On this basis, the Mean Absolute Error (MAE) is further used to spatially average $|\bar{U}|$ over all measurement points in order to evaluate the overall performance of the simulated wind speed field:

$$MAE = \frac{1}{N} \sum_{i=1}^N |U_i^M| - |U_i^O| \quad (8)$$



Where $|U_i^M|$ and $|U_i^O|$ are the model simulated and observed resultant wind speeds at the i -th observational sensor point, and N is the total number of observational sensors. The resultant wind speed is obtained from the horizontal velocity components as $|U| = \sqrt{u^2 + v^2}$. To facilitate comparison among different experimental conditions, the wind speeds are normalized by the reference wind speed. Therefore, $|U_i^M|$ and $|U_i^O|$ are both dimensionless quantities. Smaller error values indicate better model performance.

For the quantitative evaluation of pollutant concentration simulations, three core statistical metrics are employed: fractional bias (FB), normalized mean square error (NMSE), and geometric mean bias (MG). They are defined as:

$$FB = \frac{\bar{O} - \bar{M}}{0.5(\bar{O} + \bar{M})} \quad (9)$$

$$NMSE = \frac{\overline{(O_i - M_i)^2}}{\bar{O} \cdot \bar{M}} \quad (10)$$

$$MG = \exp\left(\overline{(\ln O_i)^2} - \overline{(\ln M_i)^2}\right) \quad (11)$$

where \bar{O} and \bar{M} denote the arithmetic mean of observed and simulated values, respectively. FB measures systematic bias, NMSE reflects the random scatter between simulations and observations, and MG assesses the agreement in order of magnitude. According to established atmospheric model evaluation standards (COST Action ES1006, 2015), the ideal values for these metrics are $|FB| = 0$, $NMSE = 0$, and $MG = 1$. A high-performance model should produce results as close as possible to these ideal values. However, given that perfect agreement is unattainable under all conditions, this study adopts an additional set of threshold criteria from the literature (COST Action ES1006, 2015; Kurppa et al., 2020; Schalau et al., 2023; Gkirmpas et al., 2024), which are summarised in **Table 2**.

Table 2. Threshold and standard reference values of Fractional Bias (FB), Normalized Mean Square Error (NMSE) and Geometric Mean bias (MG) used in model evaluation.

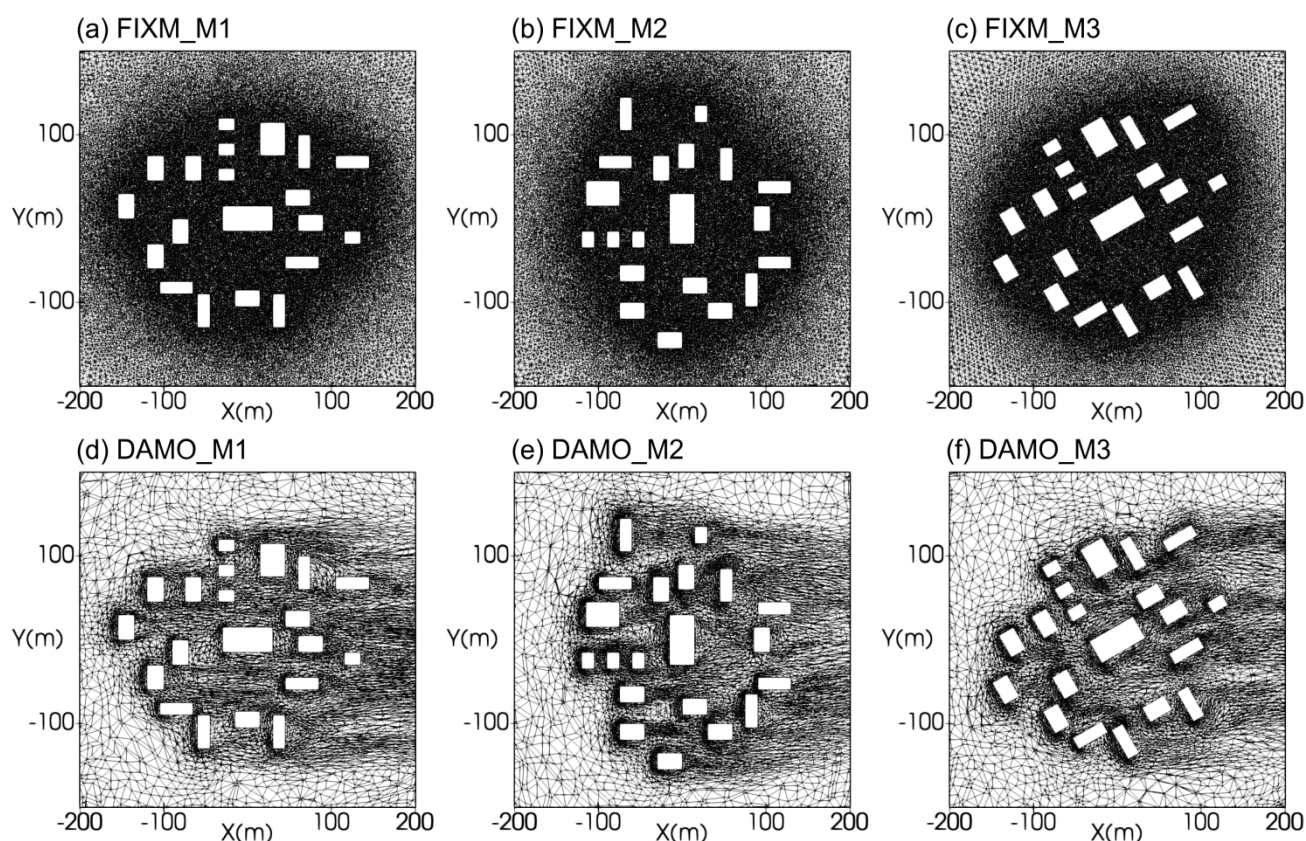
	FB	NMSE	MG
Threshold	< 0.67	< 6	0.5 < MG < 2.0
Standard	0	0	1

3 Validation results based on WTE datasets

The evaluation of FluidUrban’s simulation performance begins with an analysis of how the meshes evolves in response to complex wind flow dynamics. Benchmark comparisons are performed against the WOTAN WTE datasets to assess whether the DAMO accurately identifies and resolves the physical structures of interest. We first characterize the divergence between

the FIXM and DAMO configurations. Taking the HR experiments as an example (Figure 5), the fundamental divergence between these two types of meshes lies in the logic of computational resource allocation. The FIXM (Figure 5a–c) employs an a priori static refinement. In such configuration, the resolution is predetermined and remains invariant, regardless of the transient nature of the flow or the development of turbulence. In contrast, the DAMO mesh (Figure 5d–f) uses an a posteriori refinement mechanism, which automatically detects high gradient regions of the flow field, such as wake zones behind buildings, separated shear layers, and vortex cores, and allocates computational cells dynamically and locally to these key regions.

310



315

Figure 5: The horizontal distributions of meshes at 2 m height for FIXM (upper row) and DAMO (lower row) simulations with inflow angles of 0° (left column), 90° (middle column) and 30° (right column) for M1, M2 and M3, respectively.

To further check the 3D mesh adaptivity on the vertical distribution of the mesh, the vertical cross-sections presented in Figure 6, which provide a clear diagnostic of how the 3D DAMO framework dynamically responds to the evolving flow field in vertical direction. While the FIXM (Figure 6a–c) maintains a rigid, static resolution that ignores the development of the wake,

320



the DAMO (Figure 6d–f) exhibits a sophisticated a posteriori evolution. As the flow interacts with the building clusters, the refinement algorithm autonomously identifies the formation of separated shear layers and their subsequent downstream propagation. This is particularly evident in the extended wake regions, where DAMO maintains a high density mesh to resolve the turbulent kinetic energy and velocity deficits that characterize the downstream flow. This ability to track the flow evolution ensures that the complex building-atmosphere interactions, which are often lost in static, coarse-grid regions, are captured with high numerical fidelity. Consequently, the DAMO configuration provides a more physically consistent representation of the downstream transport of momentum and scalars compared to the fixed-mesh baseline.

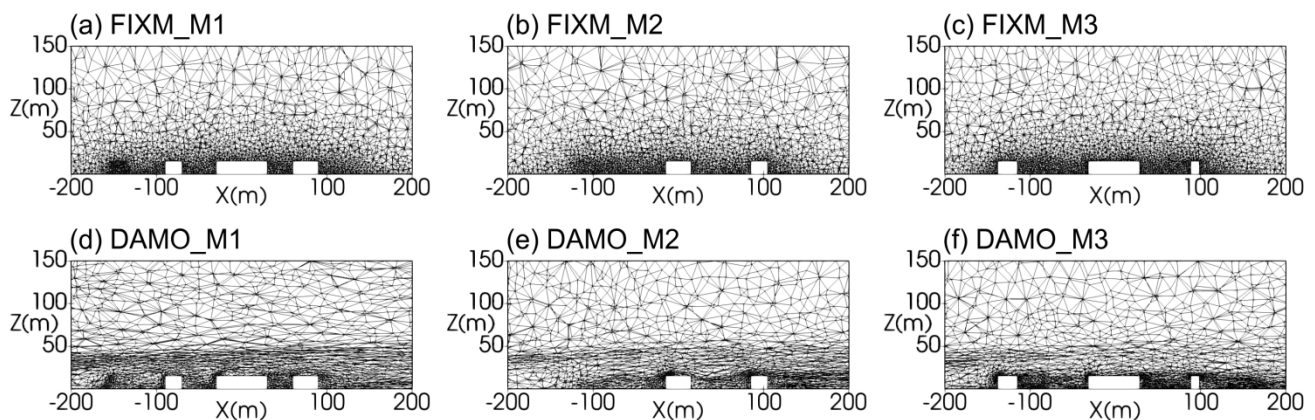


Figure 6: The z - x cross-section of meshes at $y=0$ m for FIXM (upper row) and DAMO (lower row) simulations with inflow angles of 0° (left column), 90° (middle column) and 30° (right column) for M1, M2 and M3, respectively.

3.1 wind speed

To evaluate the improvement in performance achieved by the DAMO in urban wind speed simulation, the spatial distributions of ME for horizontal wind speed ($|\bar{U}|$) at 2 m height are presented. These are shown for both MR and HR conditions in Figure 7 and Figure 8, respectively. In MR condition (Figure 7), the DAMO simulations generally exhibit lower MAE values across most regions. Particularly, in the MR-M2 case, the ME values of DAMO simulations in the vicinity of buildings are mostly confined within ± 0.1 , whereas the FIXM simulations shows significantly higher deviations in the same areas. And also, in the oblique inflow case MR-M3, the adaptive meshes refine dynamically along the shear and wake directions (Figure 5f, Figure 6f), tracking the critical flow paths to maintain high accuracy (Figure 7f). Additionally, the absolute difference of ME between the DAMO simulations and the FIXM simulations was computed (Figure 7i), where more negative values indicate smaller errors in the DAMO results. However, in the MR-M1 case, the DAMO simulation exhibits limited improvement over the FIXM simulation. This is likely because the primary inlet flow direction of 0° aligns parallel to the street canyon, generating a stable canyon flow with weak gradient that diminishes the need for adaptive refinement. Therefore, for both the MR-M1 and HR-M1 cases, the error bounds for all three velocity components were set to 0.1 to optimize simulating performance. In



addition, the errors at all observation points were further averaged to calculate the MAE, which was then used to quantitatively assess the performance of DAMO in urban wind speed simulations. Consistent with the spatial distribution results, the DAMO simulations in the MR-M2 and MR-M3 cases show a significant reduction in MAE. In the MR-M1 case, however, the MAE increases slightly, while the difference remains within approximately 0.03.

350

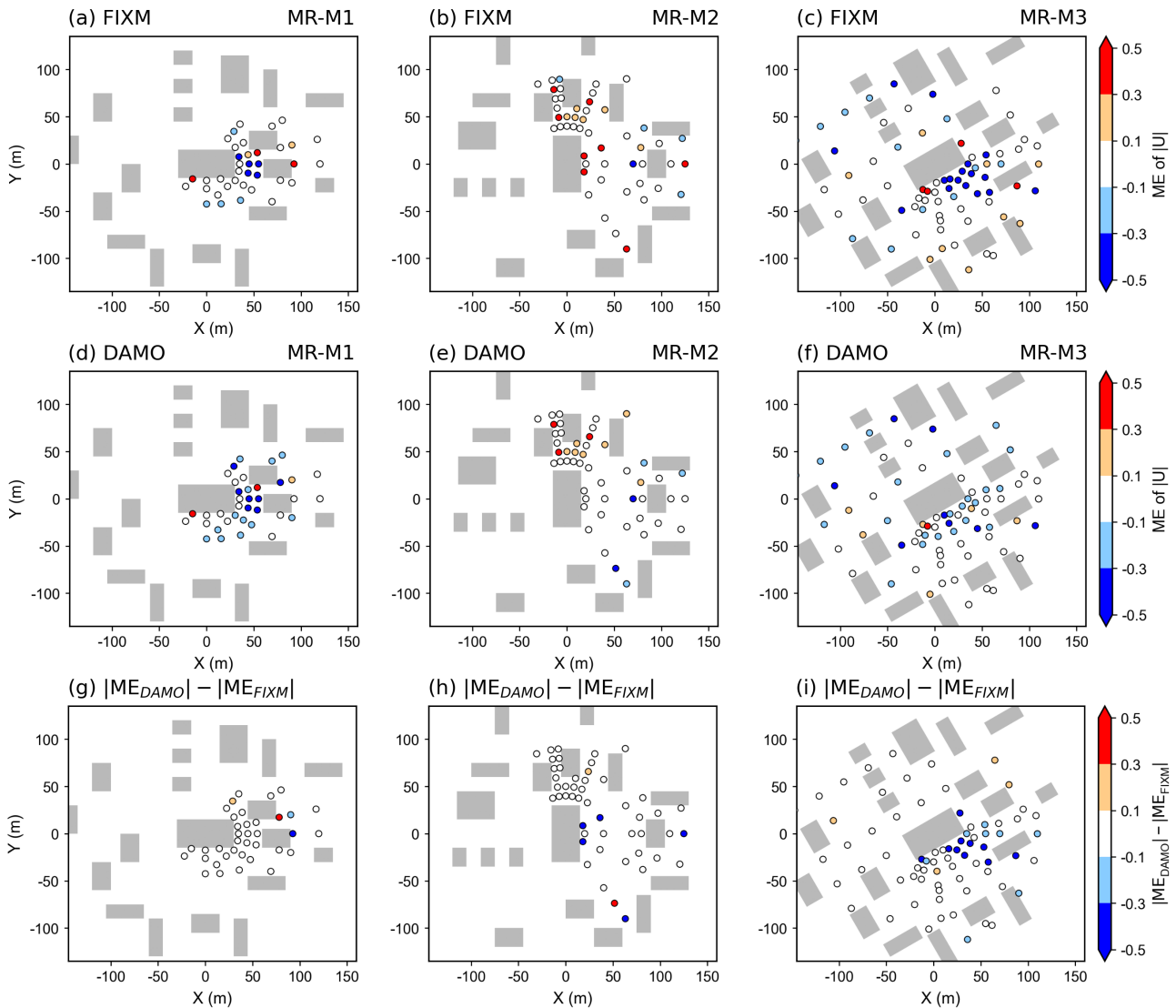


Figure 7: Spatial distribution of the Mean Error (ME) for 2 m horizontal wind speed under the medium roughness (MR) condition from FIXM (upper row) and DAMO (middle row) simulations, and the difference between the two simulations (lower row), with inlet flow direction of 0° (left column), 90° (middle column) and 30° (right column). The circle marks indicate the locations of the observational sensors in WOTAN wind tunnel experiments.

355



Table 3. Spatially averaged Mean Absolute Error (MAE) of 2 m horizontal wind speed. In each case, the smaller error between the FIXM and DAMO simulations is shown in bold.

Case	FIXM	DAMO
MR-M1	0.170	0.191
MR-M2	0.165	0.133
MR-M3	0.224	0.144
HR-M1	0.214	0.245
HR-M2	0.205	0.169
HR-M3	0.305	0.239
Average	0.214	0.187

360

The transition from MR condition (**Figure 7**) to HR condition (**Figure 8**) results in a marked decline in the overall accuracy of both the FIXM and DAMO approaches. This decline is likely attributed to the intensified interaction between the incoming turbulence and the dense building canopy under high surface roughness conditions, which generates smaller and more energetic turbulent structures that impose higher demands on the mesh resolution. Despite such challenges, the DAMO maintains superior error control in critical regions such as building wakes, confirming its robustness in complex flows. Furthermore, as

365

quantified in **Table 3**, the DAMO simulations under HR conditions achieve lower MAE for the inlet flow directions of 90° (HR-M2) and 30° (HR-M3), consistent with the MR conditions. In particular, in the HR-M3 case, the DAMO shows an error reduction of nearly 0.07. This consistent performance across various conditions further confirms the robustness of the DAMO method.

370

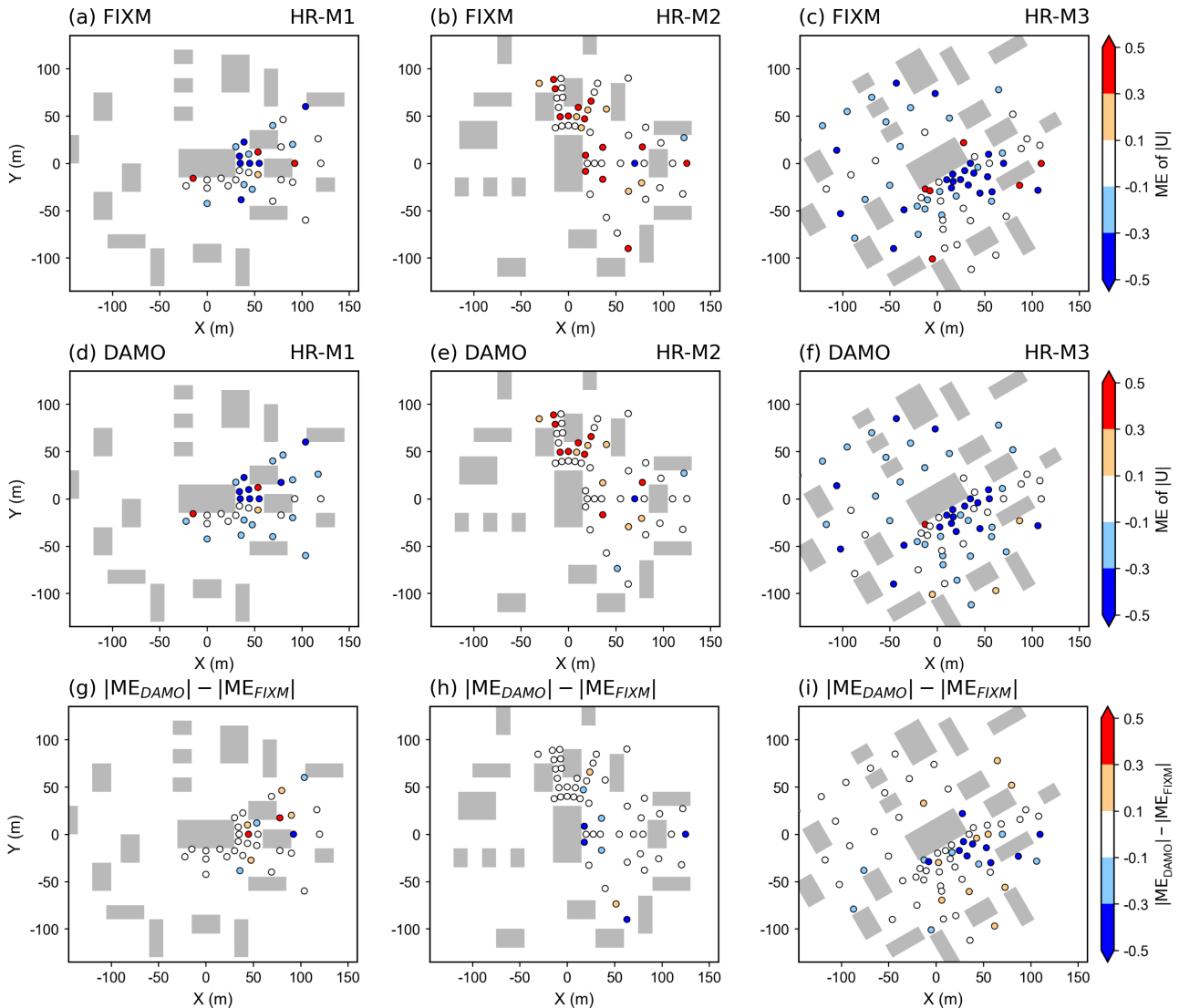


Figure 8: As in Figure 7, but for high roughness (HR) conditions.

3.2 Wind direction

Following the evaluation of wind speed, this subsection assesses the performance of DAMO in simulating wind direction.

375

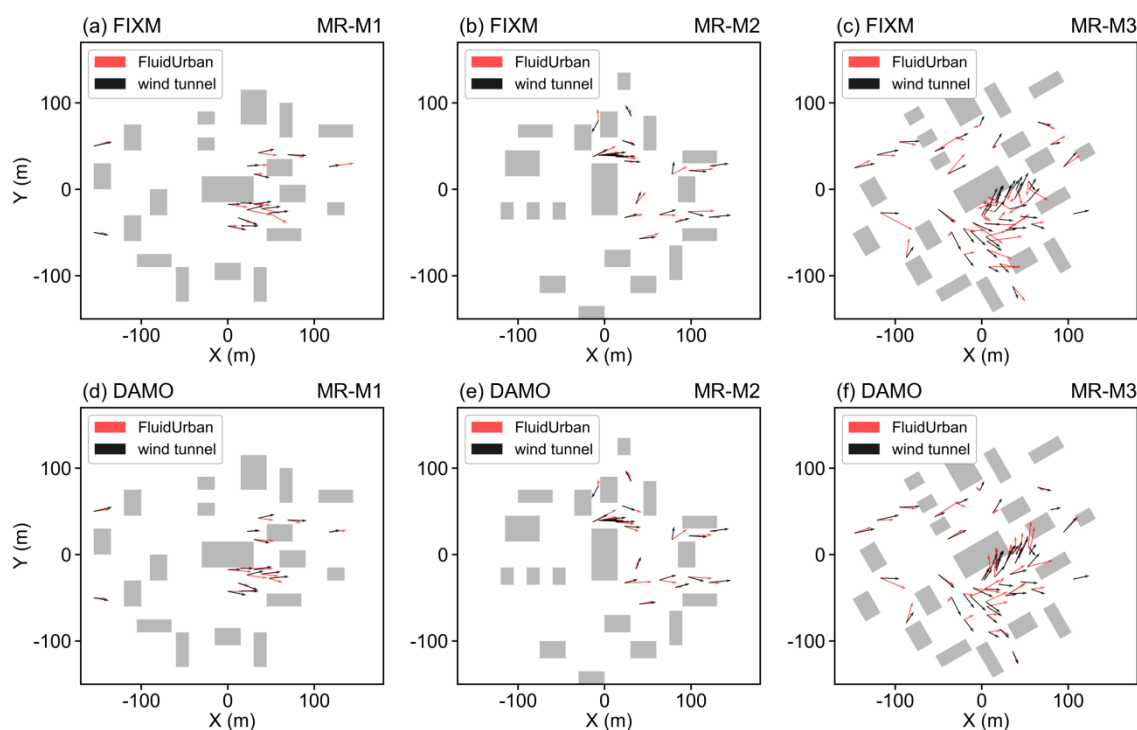
Figure 9 (MR) and Figure 10 (HR) present a visual comparison between the near-surface (2m) wind vector fields from the simulations and WTE datasets, illustrating the ability of two mesh types to resolve local flow patterns.

In the M1 and M2 cases (0° and 90°), the improvement of DAMO against FIXM is not particularly pronounced, probably due to the fact that, for inflow directions aligned with the main street axes, the near-surface airflow is primarily governed by relatively steady channelling effects and fixed velocity gradients. In contrast, in the M3 case (inflow angle of 30°), a more



380 realistic and complex scenario, the DAMO results are much closer to the WTE measurements. DAMO automatically identifies
and refines critical zones such as building windward corners and lateral separation regions, where strong pressure gradients
and momentum fluxes determine the local wind deflection. A quantitative assessment based on MAE of wind direction further
confirms the performance of DAMO. Similar to the spatial distribution, for the M3 case, DAMO reduces the MAE by 38.4%
and 36.1% for MR and HR simulations, respectively (**Figure 11**), underscoring its reliability in simulating realistic urban wind
385 fields. Although the improvement is more modest for the M1 and M2 cases (0° and 90°), DAMO still achieves a reduction in
wind direction MAE of up to 20.5%.

The advantage of DAMO is more significant for wind direction simulation compared to wind speed simulation, as wind
direction is largely governed by local velocity gradients and vorticity, which are precisely the flow structure targeted by the
DAMO refinement criteria. Moreover, accurately resolving these fine vortex structures is crucial for realistic pollutant
390 dispersion modelling, which will be explored in the following section.



395 **Figure 9: 2 m horizontal wind vectors under the medium roughness (MR) condition of the simulation (red arrows) with wind-tunnel experiment (black arrows). (a–c) present the FIXM simulation results, and (d–f) mean the DAMO simulation results, with inlet flow direction of 0° (left column), 90° (middle column) and 30° (right column).**

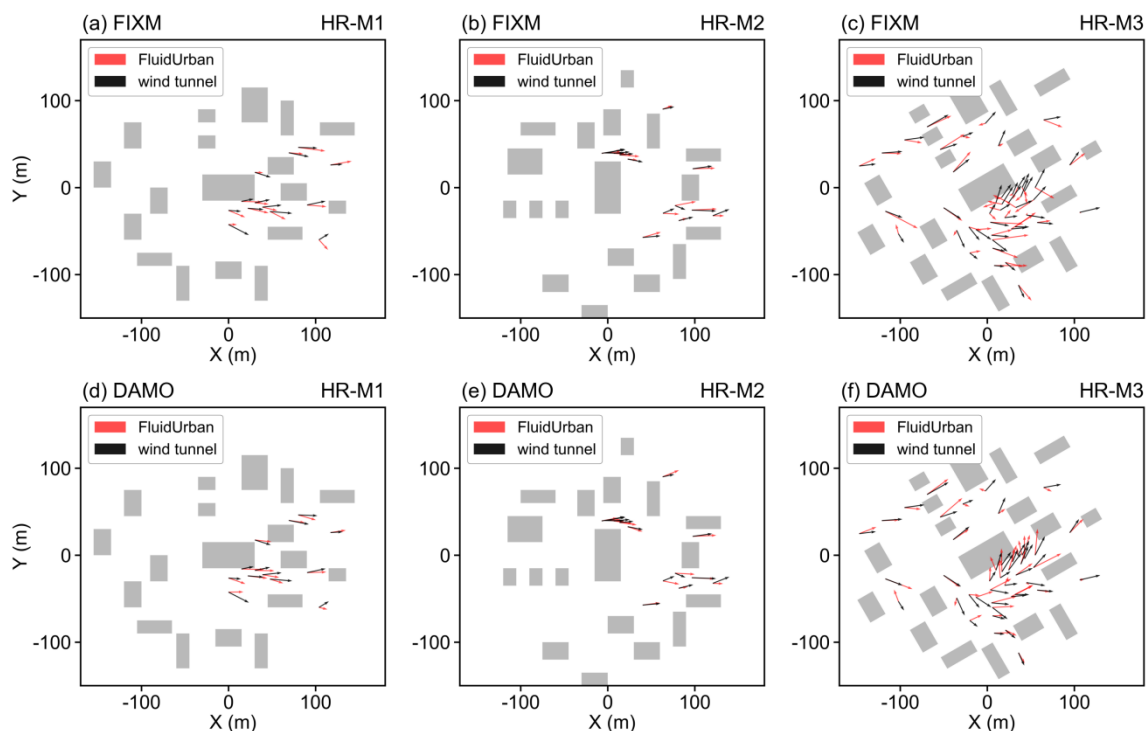


Figure 10: Same as Figure 9, but under high roughness (HR) conditions.

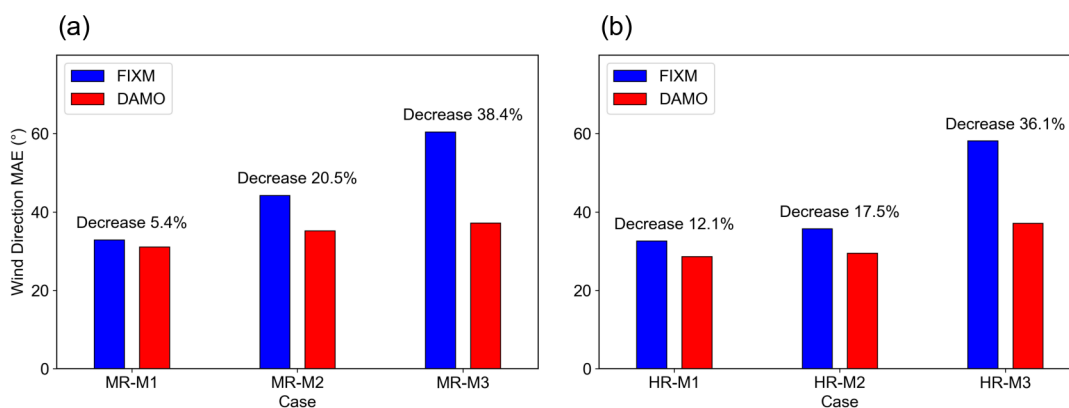


Figure 11: The spatially averaged Mean Absolute Error (MAE) of 2 m horizontal wind direction under (a) Medium roughness condition (MR) and (b) High roughness condition (HR). The labels “Decrease” and the associated percentages represent the reduction in MAE achieved by DAMO relative to FIXM.

3.3 Pollutant Dispersion

405 This section evaluates the improvement in pollutant dispersion performance achieved with DAMO. Spatial comparisons of
 plume distributon under MR and HR conditions are shown in Figure 12 and Figure 13. For inflow cases M1 and M2, the
 FIXM simulations exhibit pronounced numerical diffusion, resulting in smeared concentration gradients and excessive dilution.
 In contrast, DAMO effectively reduces this non-physical spreading and capture the sharpe gradient of pollutant concentration,
 resulting in notable improvements in plume trajectory and concentration distribution (Figure 12a, b; Figure 13a, b). The
 410 advantage of the adaptive approach is most evident in M3, where DAMO accurately resolves the governing flow structures
 and successfully reproduces the entrainment of the plume into building wake vortices, accompanied by a large angle deflection
 (Figure 12c; Figure 13c).

Further quantitative assessment employs three complementary statistical metrics: FB, NMSE, and MG (Table 4). DAMO meets
 the COST Action ES1006 acceptance criteria in 89 % of cases (16 of 18 metrics meeting thresholds), significantly exceeding
 415 the 50 % compliance rate of FIXM (9 of 18). The most pronounced contrast occurs for NMSE, a metric highly sensitive to
 extreme deviations, where DAMO outperforms FIXM in all six cases. This advantage arises from the framework’s physical
 driven allocation of computational resources, which concentrates mesh refinement in dynamically critical regions, thereby
 reducing local errors and numerical scatter. The resulting improvement in predictive stability confirms the superior accuracy
 and reliability of DAMO for urban pollutant dispersion simulations.

420

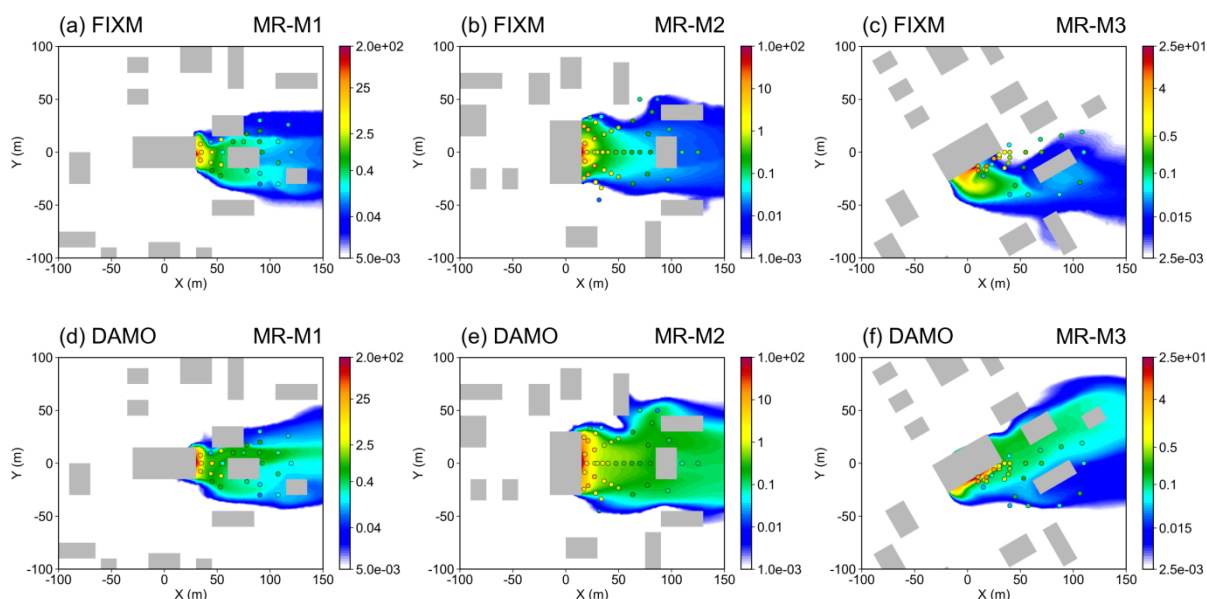


Figure 12: Pollutant gas concentration slice at 2 m above ground under medium surface roughness (shaded, units: kg m^{-3}). Gray boxes represent buildings, and the circles represent experimental measuring points. (a–c) the simulation results of FIXM, and (d–f) the simulation results of DAMO, same hereafter.



425

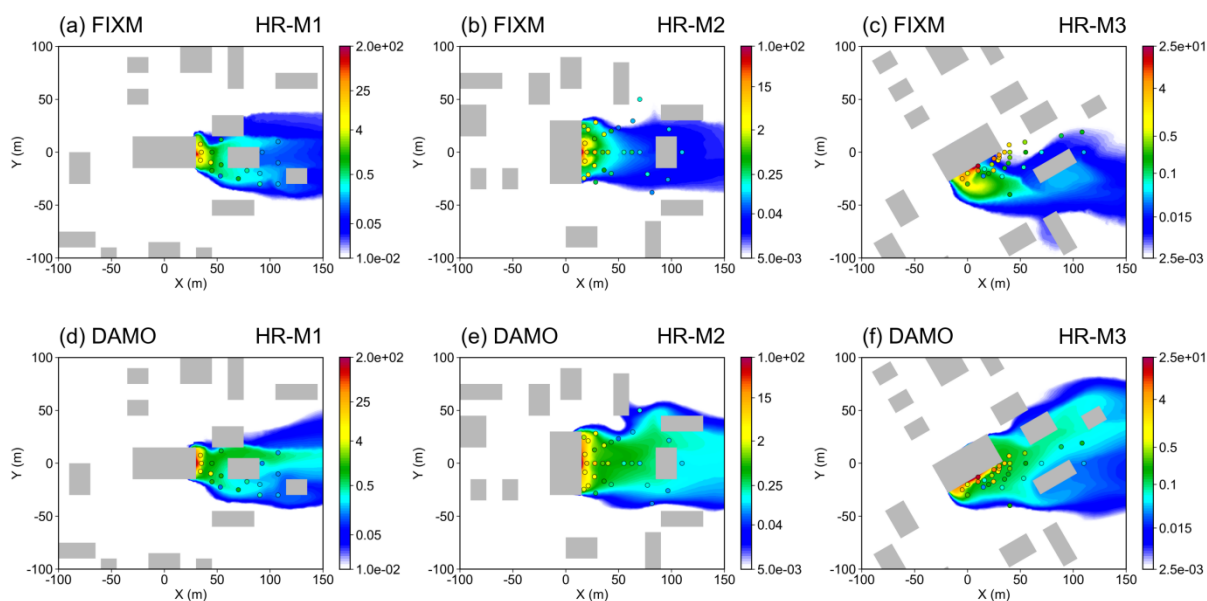


Figure 13: Same as Figure 12, but under high roughness (HR) conditions.

430

Table 4. Quantitative performance indicators for pollutant gas dispersion for all investigated cases for FIXM and DAMO. Gray shading denotes threshold-compliant indicators, bold values indicate results closer to the standard, and "Better counts" is the number of indicators closer to the standard per case.

Case	FB		NMSE		MG	
	FIXM	DAMO	FIXM	DAMO	FIXM	DAMO
MR-M1-S2	0.53	0.07	3.43	1.40	0.34	0.63
MR-M2-S1	0.58	0.18	9.63	4.15	4.29	1.30
MR-M3-S1	0.54	0.60	14.15	11.49	1.28	1.36
HR-M1-S2	0.59	0.48	3.59	2.52	0.19	0.59
HR-M2-S1	0.05	0.01	7.70	3.53	1.40	0.77
HR-M3-S1	0.71	0.59	18.74	4.11	4.90	2.56
Better counts	1	5	0	6	1	5

3.4 Computational Performance

The comparison of computational efficiency in this study is based on the current FIXM and DAMO simulations, which already exhibit a high level of consistency in their overall morphological distributions. In the DAMO, the mesh resolution dynamically evolves with the flow field; accordingly, the number of mesh nodes was documented at three representative time stages: the

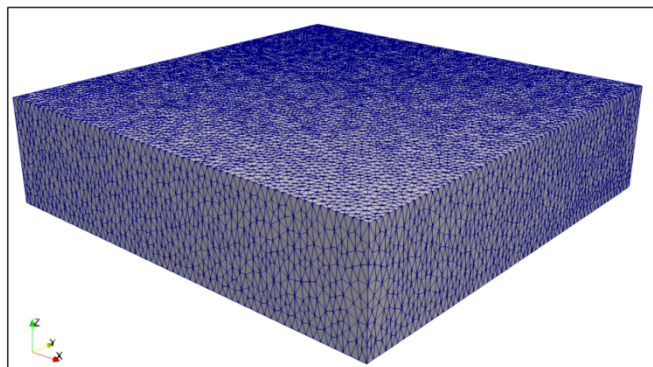
435



initial stage ($t = 0$ s), the intermediate stage ($t = 1000$ s), and the final stage ($t = 2000$ s). For the FIXM, the total number of nodes remains constant throughout the entire simulation (Table 5). From the perspective of spatial resource allocation (Figure 14), the DAMO method computational nodes are concentrated precisely within plume zones exhibiting strong concentration gradients in near-surface regions critical for pollutant dispersion ($z = 2$ m and $z = 20$ m), while dynamically adds mesh elements to better capture the fully developed flow structures in these regions in the upper-layer space above the buildings ($z = 40$ m). Considering that the total model domain height (150 m) is much greater than the building height (15 m), such enhanced resolution of the upper-layer flow results in a slightly higher total number of nodes for the DAMO during the late simulation period.

Although dynamic adaptivity offers significant advantages in accuracy, it also introduces extra computational cost for mesh adjustment. At present, the DAMO simulations employ 299,186 cells and require 333 minutes to complete, whereas the FIXM uses 238,905 cells and finishes in 227 minutes. When normalized to an equivalent number of mesh points, the DAMO exhibits an approximately 17.1% longer total simulation time compared with the FIXM. This quantifiable overhead highlights the “deliberate computational investment” undertaken to achieve higher physical realism and resolve complex flow structures, while underscoring the continued need for algorithmic optimization to further improve computational efficiency without compromising accuracy. Future work may consider applying moderate mesh coarsening in the upper-layer regions, thereby allocating more computational resources to the near-ground critical areas to further enhance overall model performance.

(a) FIXM



(b) DAMO

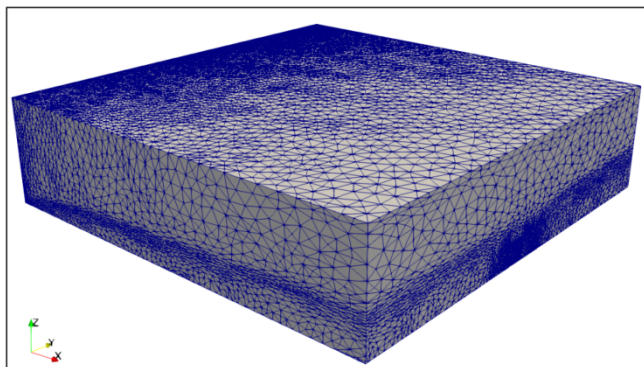


Figure 14: Comparison of 3D model meshes generated by the FIXM (left) and DAMO (right) methods.



460

Table 5. Comparison of mesh cell numbers and running times in the simulation experiments. The table lists the mesh cell numbers for DAMO and FIXM at different height sections as well as for the entire computational domain. For the DAMO, the mesh cell numbers are recorded at different simulation times. “Times” indicates the total running time for each of the two mesh configurations.

	DAMO			FIXM
	$t = 0$ s	$t = 1000$ s	$t = 2000$ s	
$z = 2$ m	215643	39692	39618	102737
$z = 20$ m	100920	40705	40050	53225
$z = 40$ m	60347	29660	29247	30833
$z = 60$ m	40560	26721	26489	21388
$z = 80$ m	29091	26496	26652	18045
Domain	358312	311738	299186	238905
Times	333 min			227 min

4 Realistic urban scenario simulation

465

To further check its performance in a realistic application, FluidUrban was employed to simulate the wind field over the Industrial Park of Zhenhai Refining and Chemical Company (ZRCC) in Ningbo, Zhejiang Province, China. The 3D geometry of the Industrial Park was reconstructed using the approach described in Section 2.1.1, and the corresponding computational domain and mesh was subsequently simulated using the DAMO method (**Figure 1**).

470

At the inlet, a northerly inflow was specified according to the climatological prevailing wind direction in winter around the Industrial Park. The mean streamwise inflow profile $\bar{U}_{in}(z)$ was defined as a function of the vertical coordinate z and followed the standard logarithmic law above the roughness height z_0 , as given in Eq. (12), while the remaining flow components were set to zero. At the outlet, a zero-stress condition was applied and the pressure was fixed at 0 to allow the flow to develop freely. No-slip boundary conditions were imposed on the ground and building surfaces. The lateral boundaries and the top boundary were treated as symmetry planes with slip conditions, thereby alleviating the need to resolve far-field flow details. The wind field was then simulated using the DAMO method. DAMO was employed with grid sizes ranging from 2 m to 1000 m; with a dynamical updated frequency of every 10 time steps, and the time step was also dynamically adaptive under a CFL constraint of 5.



475
$$\bar{U}_{in}(z) = \begin{cases} 0, & z < z_0, \\ \frac{u_*}{\kappa\alpha} \ln\left(\frac{z}{z_0}\right), & z \geq z_0, \end{cases} \quad (12)$$

where u_* is the friction velocity and $\kappa\alpha = 0.41$ is the von Karman constant. In this study, $u_* = 0.4$, corresponding to a wind speed of approximately 2.4 m s^{-1} at $z = 10 \text{ m}$ based on the climatological winter wind speed over the Industrial Park, and the roughness length was set to $z_0 = 0.84 \text{ m}$. After the flow reached a statistically steady state, the simulated wind field over the entire computational domain is presented in **Figure 15a**. Under the complex morphology of the industrial park, the model resolves the pronounced spatial heterogeneity of the wind field caused by blocking and channeling effects. A close-up analysis of the flow field (**Figure 15b**, zooming in on the region indicated in **Figure 15a**) reveals distinct turbulent disturbances within and leeward of dense building clusters. This confirms the capacity of the FluidUrban 1.0 framework to accurately represent sub-grid scale flow structures within complex building arrays.

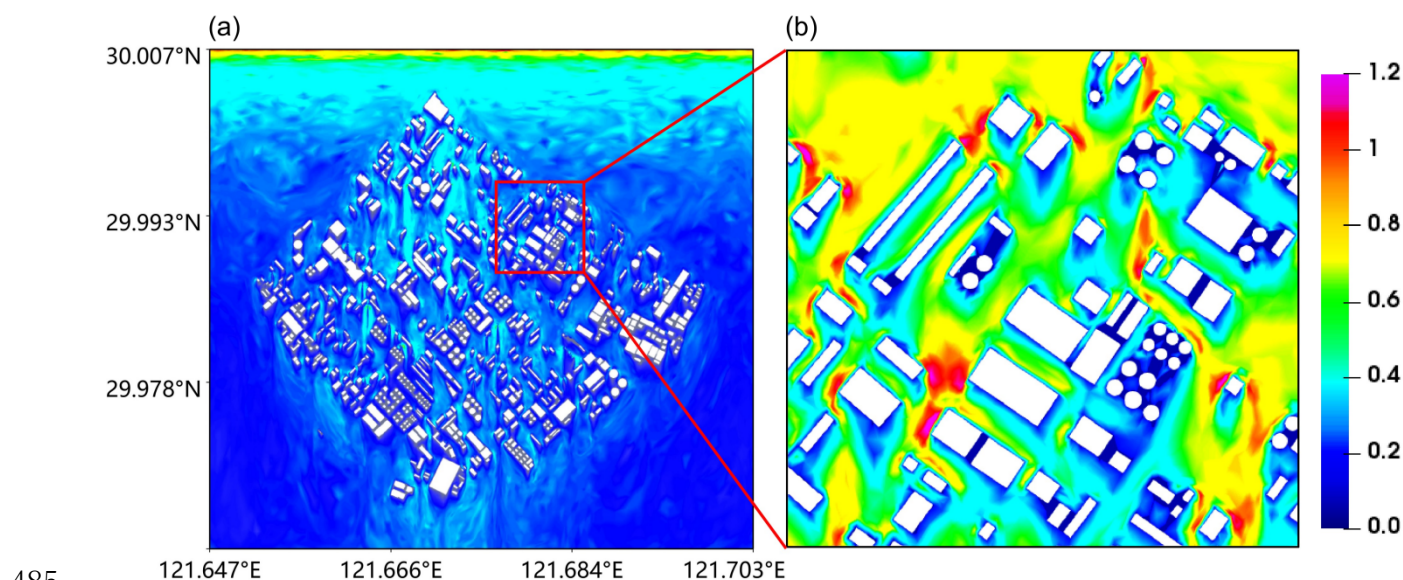


Figure 15: Spatial distribution of the 10m wind field magnitude (m s^{-1}) simulated by FluidUrban 1.0 for the realistic urban scenario:(a) full-domain overview and (b) detailed subset of the region indicated in (a).

5 Conclusions

This study introduces and systematically evaluates FluidUrban v1.0, an advanced urban environmental modelling framework built upon the open-source Fluidity solver. The core methodological advancement of this research is the development of a dedicated 3D urban geometry and unstructured mesh generator, which is coupled with urban-specific boundary conditions. This integration establishes a robust foundation for explicitly resolving complex urban morphologies and driving the 3D DAMO algorithm. To comprehensively quantify the advantages of this adaptive framework, the model was validated against

490



495 the high-fidelity WOTAN WTE datasets, investigating both urban flow and pollutant dispersion under varying surface roughness conditions and inflow directions. The principal findings of this study are summarized as follows:

(1) Model Development and Initialisation: The integration of the newly developed geometry and mesh generator ensures that FluidUrban v1.0 can accurately initialize complex physical boundaries. During simulations, the DAMO algorithm effectively identifies evolving flow physics and pollutant concentration and dynamically refines or coarsens the computational grid, concentrating resources strictly in dynamically critical regions

500 (2) Wind Speed Simulation: the DAMO framework consistently outperformed traditional non-uniform fixed meshes (FIXM) by capturing complex urban wind fields more accurately. On average, DAMO achieved a MAE of 0.187, significantly lower than the 0.214 obtained by FIXM. Performance gains were most pronounced in oblique inflow scenarios (M3), whereas under flow conditions parallel to street canyons, the difference in errors between the two methods was relatively small due to the higher stability of the flow gradients.

505 (3) Wind Direction Simulation: the DAMO frame work showed a clear advantage in simulating local flow patterns and deflections around building structures. For realistic 30° tilted inflow conditions (M3), DAMO reduced the MAE of wind direction by 38.4% in MR conditions and 36.1% in HR conditions. This accuracy is attributed to the model's ability to automatically identify and refine mesh resolution at building corners and lateral separation regions where pressure gradients are highest.

510 (4) Pollutant Dispersion: DAMO successfully reproduced plume trajectories and the entrainment of pollutants into building-wake vortices. While fixed meshes often produced blurred boundaries and excessive numerical diffusion, the DAMO approach produced sharply defined plume contours and suppressed non-physical spreading. Quantitatively, the DAMO simulations achieved an 89% compliance rate (16 out of 18) with established atmospheric model evaluation standards (FB, NMSE, and MG), significantly exceeding the 50% compliance rate of FIXM simulations.

515 (5) Accuracy-Efficiency Balance: although DAMO introduces additional runtime cost due to the iterative mesh regeneration process, this cost is strategically offset by its ability to concentrate computational resources only where needed. The results confirm that DAMO provides a superior balance between accuracy and computational demand compared to globally refined fixed meshes.

Beyond idealized benchmarks, the practical utility of the model was demonstrated through a realistic urban scenario simulation.

520 The results confirm that FluidUrban v1.0 successfully resolves the pronounced spatial heterogeneity and complex channeling effects inherent to authentic city morphologies. By dynamically tracking flow evolution within dense building clusters and their downstream regions, the DAMO framework provides a high-fidelity representation of realistic urban ventilation patterns that are often unresolved by static mesh approaches. In conclusion, FluidUrban v1.0 proves to be a robust and highly accurate tool for resolving the transient, small-scale flow structures that dictate urban pollutant transport. By successfully maintaining sharp concentration gradients, the framework offers significant potential for high-fidelity exposure assessments in urban air quality studies. In its current scope, v1.0 is intentionally designed as an aerodynamic and scalar-transport baseline. Moving forward, future development will proceed in two main directions. First, we will continue to optimize the DAMO algorithm to

525



530 further reduce runtime over complex building clusters. Second, to transition from a ventilation tool to a comprehensive urban model, we have already begun the integration of major urban physical components—including radiation, vegetation, and energy-balance physics. These extensions will be formally introduced in the upcoming FluidUrban v1.1. The combination of these future extensions with DAMO’s capability to capture sharp thermal and chemical gradients will be essential for modeling urban multiscale physical processes and complex air quality events.

Code and data availability

535 The FluidUrban v1.0 used in this study, a specialized derivative of the Fluidity framework, is archived on Zenodo (<https://doi.org/10.5281/zenodo.19334189>; Wu et al., 2026a). The 3D urban geometry and mesh generator, model output data reported in this paper, and the plotting scripts are archived on Zenodo (<https://doi.org/10.5281/zenodo.19221580>; Wu et al., 2026b). The wind-tunnel data is from Hamburg University (<https://www.mi.uni-hamburg.de/en/arbeitsgruppen/windkanallabor/data-sets.html>).

Competing interests

540 The contact author has declared that none of the authors has any competing interests.

Disclaimer

545 Publisher's note: Copernicus Publications remains neutral with regard to jurisdictional claims made in the text, published maps, institutional affiliations, or any other geographical representation in this paper. The authors bear the ultimate responsibility for providing appropriate place names. Views expressed in the text are those of the authors and do not necessarily reflect the views of the publisher.

Author contributions.

550 WX: Conceptualization, Data curation, Funding acquisition, Investigation, Methodology, Resources, Software, Supervision, Validation, Visualization, Writing (review and editing). CS: Conceptualization, Data curation, Formal analysis, Investigation, Methodology, Software, Visualization, Writing (original draft preparation). LJ: Data curation, Investigation, Validation, Writing (review and editing). ZY, WZ: Conceptualization, Project administration, Resources, Validation, Writing (review and editing). GP, ZJ: Software, Validation, Writing (review and editing). FF: Data curation, Investigation, Validation, Writing (review and editing).

Acknowledgement

560 Wu thank for the technical support of the National Large Scientific and Technological Infrastructure “Earth System Numerical Simulation Facility”(grant no. 2025-EL-PT-000922, <https://cstr.cn/31134.02.EL>) and wind-tunnel data support of Hamburg University (<https://www.mi.uni-hamburg.de/en/arbeitsgruppen/windkanallabor/data-sets.html>).

Financial support

565 Wu would like to thank for supporting funding form the National Key Research and Development Program of China (grant no. 2023YFC3705702) and the Chengdu Science and Technology Program (grant no. 2025-XT00-00001-GX). Fang would like to thank for supporting funding from Engineering and Physical Sciences Research Council (EPSRC) ([EP/X029093/1](https://www.ukri.org/projects/ep/x029093/1)).

References

570 AMCG: Fluidity Manual, Applied Modelling and Computation Group, Imperial College London, <https://github.com/FluidityProject/fluidity>, 2014.

Apte, J. S. and Manchanda, C.: High-resolution urban air pollution mapping, *Science*, 385, 380–385, doi:10.1126/science.adq3678, 2024.

Arafa, M. A. and Zinat, A.: Comprehensive Validation of RANS-Based Urban Wind Flow Simulations using the ‘Michel-Stadt’ Benchmark, *Journal of Studies in Civil Engineering*, 2, 22–34, doi:10.53898/jsce2025222, 2025.

575 Badach, J., Dymnicka, M., and Baranowski, A.: Urban vegetation in air quality management: A review and policy framework, *Sustainability*, 12, 1258, doi:10.3390/su12031258, 2020.

Bauer, H. S., Muppa, S. K., Wulfmeyer, V., Behrendt, A., Warrach-Sagi, K., and Späth, F.: Multi-nested WRF simulations for studying planetary boundary layer processes on the turbulence-permitting scale in a realistic mesoscale environment, *Tellus A*, 72, 1–28, doi:10.1080/16000870.2020.1761740, 2020.

580 Connerton, P., Vicente de Assunção, J., Maura de Miranda, R., Dorothée Slovic, A., José Pérez-Martínez, P., and Ribeiro, H.: Air quality during COVID-19 in four megacities: lessons and challenges for public health, *Int. J. Environ. Res. Public Health*, 17, 5067, doi:10.3390/ijerph17145067, 2020.

COST Action ES1006: Best practice guidelines: Evaluation, improvement and guidance for the use of local-scale emergency prediction and response tools for airborne hazards in built environments, 2015.

585 Cui, P., Li, Z., and Tao, W.: Buoyancy flows and pollutant dispersion through different scale urban areas: CFD simulations and wind-tunnel measurements, *Build. Environ.*, 104, 76–91, doi:10.1016/j.buildenv.2016.04.028, 2016.

da Silva, F. T., Reis Jr, N. C., Santos, J. M., Goulart, E. V., and de Alvarez, C. E.: The impact of urban block typology on pollutant dispersion, *Journal of Wind Engineering and Industrial Aerodynamics*, 210, 104524, doi:10.1016/j.jweia.2021.104524, 2021.

590 Di Sabatino, S., Buccolieri, R., and Salizzoni, P.: Recent advancements in numerical modelling of flow and dispersion in urban areas: a short review, *Int. J. Environ. Pollut.*, 52, 172–191, doi:10.1504/IJEP.2013.058454, 2013.



Farrell, P. E., Piggott, M. D., Pain, C. C., Gorman, G. J., and Wilson, C. R.: Conservative interpolation between unstructured meshes via super mesh construction, *Comput. Methods Appl. Mech. Engrg.*, 198, 2632–2642, doi:10.1016/j.cma.2009.03.004, 2009.

595 Franke, J., Hellsten, A., Schlunzen, K. H., and Carissimo, B.: The COST 732 Best Practice Guideline for CFD simulation of flows in the urban environment: a summary, *Int. J. Environ. Pollut.*, 44, 419–427, doi:10.1504/IJEP.2011.038443, 2011.

Fuller, E. N., Schettler, P. D., and Giddings, J. C.: New method for prediction of binary gas-phase diffusion coefficients, *Ind. Eng. Chem.*, 58, 18–27, doi:10.1021/ie50677a007, 1966.

600 Giani, P. and Crippa, P.: On the Sensitivity of Large-Eddy Simulations of the Atmospheric Boundary Layer Coupled with Realistic Large-Scale Dynamics, *Mon. Weather Rev.*, 152, 1057–1075, doi:10.1175/MWR-D-23-0101.1, 2024.

Gkirmpas, P., Barmpas, F., Tsegas, G., Efthimiou, G., Tremper, P., Riedel, T., Vlachokostas, C., and Moussiopoulos, N.: An Evaluation of the Sensitivity of a Source Term Estimation Methodology of Sensor Configuration in an Urban-like Environment, *Atmosphere*, 15, 1512, doi:10.3390/atmos15121512, 2024.

605 Gromke, C.: A vegetation modeling concept for building and environmental aerodynamics wind tunnel tests and its application in pollutant dispersion studies, *Environ. Pollut.*, 159, 2094–2099, doi:10.1016/j.envpol.2010.11.012, 2011.

Han, C., Hoose, C., Stengel, M., Coopman, Q., and Barrett, A.: Sensitivity of cloud phase distribution to cloud microphysics and thermodynamics in simulated deep convective clouds and SEVIRI retrievals, *Atmos. Chem. Phys.*, 23, 14077–14095, doi:10.5194/acp-23-14077-2023, 2023.

610 Hang, J., Luo, Z., Sandberg, M., and Gong, J.: Natural ventilation assessment in typical open and semi-open urban environments under various wind directions, *Build. Environ.*, 70, 318–333, doi:10.1016/j.buildenv.2013.09.002, 2013.

Jackson, M. D., Percival, J. R., Mostaghimi, P., Tollit, B. S., Pavlidis, D., Pain, C. C., Gomes, J. L. M. A., El-Sheikh, A. H., Salinas, P., Muggeridge, A. H., and Blunt, M. J.: Reservoir modeling for flow simulation by use of surfaces, adaptive unstructured meshes, and an overlapping-control-volume finite-element method, *SPE Reserv. Eval. Eng.*, 18, 115–132, doi:10.2118/163633-PA, 2015.

615 Khan, A., Vasilakopoulou, K., and Santamouris, M.: Exploring the potential impacts of anthropogenic heating on urban climate during heatwaves, *Sci. Rep.*, 15, 3908, doi:10.1038/s41598-024-83918-y, 2025.

620 Khan, B., Banzhaf, S., Chan, E. C., Forkel, R., Kanani-Sühring, F., Ketelsen, K., Kurppa, M., Maronga, B., Mauder, M., Raasch, S., Russo, E., Schaap, M., and Sühring, M.: Development of an atmospheric chemistry model coupled to the PALM model system 6.0: implementation and first applications, *Geosci. Model Dev.*, 14, 1171–1193, doi:10.5194/gmd-14-1171-2021, 2021.

Khomenko, S., Cirach, M., Pereira-Barboza, E., Mueller, N., Barrera-Gómez, J., Rojas-Rueda, D., de Hoogh, K., Hoek, G., and Nieuwenhuijsen, M.: Premature mortality due to air pollution in European cities: a health impact assessment, *Lancet Planet. Health*, 5, e121–e134, doi:10.1016/S2542-5196(20)30272-2, 2021.



- 625 Kurppa, M., Roldin, P., Strömberg, J., Balling, A., Karttunen, S., Kuuluvainen, H., Niemi, J. V., Pirjola, L., Rönkkö, T.,
Timonen, H., Hellsten, A., and Järvi, L.: Sensitivity of spatial aerosol particle distributions to the boundary conditions in the
PALM model system 6.0, *Geosci. Model Dev.*, 13, 5663–5685, doi:10.5194/gmd-13-5663-2020, 2020.
- Kusaka, H., Ikeda, R., Sato, T., Iizuka, S., and Boku, T.: Development of a multi-scale meteorological large-eddy simulation
model for urban thermal environmental studies: The “City-LES” model version 2.0, *J. Adv. Model. Earth Syst.*, 16,
e2024MS004367, doi:10.1029/2024MS004367, 2024.
- 630 Li, J., Li, Y., Wang, Z., Zhu, J., Kong, L., Li, J., Wu, H., Li, L., Tang, X., Cheng, Z., Zhang, L., Gan, P., Pan, X., Yang, W.,
Cao, K., and Zheng, J.: Next Generation Air Quality Models: Dynamical Mesh, New Insights into Mechanism, Datasets and
Applications, *Curr. Pollut. Rep.*, 11, 25, doi:10.1007/s40726-025-00355-9, 2025.
- Li, J., Zheng, J., Zhu, J., Fang, F., Pain, C. C., Steppeler, J., Navon, I. M., and Xiao, H.: Performance of Adaptive unstructured
Mesh Modeling in idealized Advection cases over steep Terrains, *Atmosphere*, 9, 444, doi:10.3390/atmos9110444, 2018.
- 635 Liang, W. and Zheng, X.: CFD simulation of mixed convection and pollutant dispersion in street canyons: A comparative
assessment of LES, RANS, and SAS, *Sustain. Cities Soc.*, 107126, doi:10.1016/j.scs.2026.107126, 2026.
- Liu, W., Huang, Z., Sun, M., Zhang, H., Zhao, F., and Guo, R.: Applying Numerical Simulation to Identify the Suitable Block
Scale for Improving Air Quality Inside Urban Streets, in: *International Conference on Urban Climate, Sustainability and Urban
Design*, pp. 603–616, Springer, doi:10.1007/978-981-97-8401-1_43, 2023.
- 640 Michel, S. J.: Feasibility Study of Heavy Gas Dispersion Experiments in Complex Environments in Physical Modeling,
Master's thesis, Universität Hamburg, Hamburg, Germany, 2023.
- Mottet, L., Song, J., Short, C. A., Chen, S., Wu, J., Yu, W., Xiong, J., Zhang, Q., Ge, J., Liu, M., Yao, R., and Li, B.: The hot
summer-cold winter region in China: Challenges in the low carbon adaptation of residential slab buildings to enhance comfort,
Energy Build., 223, 110181, doi:10.1016/j.enbuild.2020.110181, 2020.
- 645 Müller, A., Behrens, J., Giraldo, F. X., and Wirth, V.: Comparison between adaptive and uniform discontinuous Galerkin
simulations in dry 2D bubble experiments, *J. Comput. Phys.*, 235, 371–393, doi:10.1016/j.jcp.2012.10.038, 2013.
- Nagai, T., Hibiya, T., and Syamsudin, F.: Direct estimates of turbulent mixing in the Indonesian archipelago and its role in the
transformation of the Indonesian throughflow waters, *Geophys. Res. Lett.*, 48, e2020GL091731, doi:10.1029/2020GL091731,
2021.
- 650 Nonaka, I. T.: Modeling and simulation of multicomponent evaporative sprays in generic conditions, Master's thesis,
Universidade Federal de Uberlândia, Faculdade de Engenharia Mecânica, Uberlândia, Brazil, 2025.
- Pain, C. C., Piggott, M. D., Goddard, A. J. H., Fang, F., Gorman, G. J., Marshall, D. P., Eaton, M. D., Power, P. W., and de
Oliveira, C. R. E.: Three-dimensional unstructured mesh ocean modeling, *Ocean Model.*, 10, 5–33,
doi:10.1016/j.ocemod.2004.07.005, 2005.
- 655 Park, S. J. and Kim, J. J.: Development of a computational fluid dynamics model adopting a nested grid system: Flow
simulations for ideal and real urban settings, *Urban Clim.*, 53, 101801, doi:10.1016/j.uclim.2023.101801, 2024.

Pavlidis, D., Gorman, G., Gomes, J., Pain, C., and ApSimon, H.: Synthetic-eddy method for urban atmospheric flow modelling, *Bound.-Layer Meteorol.*, 136, 285–299, doi:10.1007/s10546-010-9508-x, 2010.

660

Pesci, C., Weiner, A., Marschall, H., and Bothe, D.: Computational analysis of single rising bubbles influenced by soluble surfactant, *J. Fluid Mech.*, 856, 709–763, doi:10.1017/jfm.2018.723, 2018.

Ricci, A., Kalkman, I., and Blocken, B.: Local-scale forcing effects on wind flows in an urban environment: Impact of geometrical simplifications, *J. Wind Eng. Ind. Aerodyn.*, 170, 238–255, doi:10.1016/j.jweia.2017.08.001, 2017.

665

Savre, J., Percival, J., Herzog, M., and Pain, C.: Two-dimensional evaluation of ATHAM-fluidity, a nonhydrostatic atmospheric model using mixed continuous/discontinuous finite elements and anisotropic grid optimization, *Mon. Weather Rev.*, 144, 4349–4372, doi:10.1175/MWR-D-15-0398.1, 2016.

Schalau, S., Habib, A., and Michel, S.: A modified k- ϵ turbulence model for heavy gas dispersion in built-up environment, *Atmosphere*, 14, 161, doi:10.3390/atmos14010161, 2023.

670

Sezen, S. and Atlar, M.: An alternative Vorticity based Adaptive Mesh Refinement (V-AMR) technique for tip vortex cavitation modeling of propellers using CFD methods, *Ship Technol. Res.*, 69, 1–21, doi:10.1080/09377255.2021.1927590, 2022.

Tarraf, A., Schreiber, M., Cascajo, A., Besnard, J.-B., Vef, M.-A., and Huber, D.: Malleability in modern HPC systems: current experiences, challenges, and future opportunities, *IEEE Trans. Parallel Distrib. Syst.*, 35, 1551–1564, doi:10.1109/TPDS.2024.3406764, 2024.

675

Tominaga, Y., Mochida, A., Yoshie, R., Kataoka, H., Nozu, T., Yoshikawa, M., and Shirasawa, T.: AIJ guidelines for practical applications of CFD to pedestrian wind environment around buildings, *J. Wind Eng. Ind. Aerodyn.*, 96, 1749–1761, doi:10.1016/j.jweia.2008.02.058, 2008.

United Nations, Department of Economic and Social Affairs, Population Division: *World Urbanization Prospects: The 2018 Revision (ST/ESA/SER.A/420)*, United Nations, New York, 2019.

680

VDI: *Environmental meteorology – Physical modelling of flow and dispersion processes in the atmospheric boundary layer – Application of wind tunnels*, VDI Standard 3783, Verein Deutscher Ingenieure, 2000.

Wang, C., Wang, W., Qu, J., Wang, Q., Wang, X., and Liu, X.: Multi-Scale Validation of CFD Simulations for Pollutant Dispersion Around Buildings, *Processes*, 13, 4076, doi:10.3390/pr13124076, 2025.

Weger, M. and Heinold, B.: Air pollution trapping in the Dresden Basin from gray-zone scale urban modeling, *Atmos. Chem. Phys.*, 23, 13769–13790, doi:10.5194/acp-23-13769-2023, 2023.

685

Wu, X., Abubakar-Waziri, H., Fang, F., Dilliway, C., Wu, P., Li, J., Yao, R., Bhavsar, P., Kumar, P., Pain, C. C., and Chung, K. F.: Modeling for understanding of coronavirus disease-2019 (COVID-19) spread and design of an isolation room in a hospital, *Phys. Fluids*, 35, 025111, doi:10.1063/5.0135247, 2023.

Wu, X., Chen, S., and Fang, F.: *FluidUrban v1.0*, Zenodo, doi:10.5281/zenodo.19334189, 2026a.



690

Wu, X., Chen, S., Li, J., Zhang, Y., Wang, Z., Gan, P., Zheng, J., and Fang, F.: FluidUrban v1.0: Enhancing Urban Ventilation and Pollutant Dispersion Modelling with Three-dimensional Dynamic Adaptive Meshes Optimization [Data set], Zenodo, doi:10.5281/zenodo.19221580, 2026b.

Yang, L., Wang, G., Wang, Y., Wang, Y., Ma, Y., and Zhang, X.: A rapid computational method for quantifying inter-regional air pollutant transport dynamics, *Atmosphere*, 16, 163, doi:10.3390/atmos16020163, 2025.

695

Yu, J., Lyu, H., Xu, R., Ouyang, W., and Liu, X.: Flow2Mesh: A flow-guided data-driven mesh adaptation framework, *Phys. Fluids*, 36, doi:10.1063/5.0188690, 2024.

Zhang, C. X., Liu, Y., Fu, B. S., and Yu, X. J.: Direct numerical simulation of subsonic–supersonic mixing layer, *Acta Astronaut.*, 153, 50–59, doi:10.1016/j.actaastro.2018.10.004, 2018.

Zheng, J., Wu, X., Fang, F., Li, J., Wang, Z., Xiao, H., Zhu, J., Pain, C., Linden, P., and Xiang, B.: Numerical study of COVID-19 spatial–temporal spreading in London, *Phys. Fluids*, 33, doi:10.1063/5.0048472, 2021.

700

Zheng, J., Zhu, J., Wang, Z., Fang, F., Pain, C. C., and Xiang, J.: Towards a new multiscale air quality transport model using the fully unstructured anisotropic adaptive mesh technology of Fluidity (version 4.1.9), *Geosci. Model Dev.*, 8, 3421–3440, doi:10.5194/gmd-8-3421-2015, 2015.

Zhong, J., Liu, J., Xu, Y., and Liang, G.: Pedestrian-level gust wind flow and comfort around a building array–Influencing assessment on the pocket park, *Sustain. Cities Soc.*, 83, 103953, doi:10.1016/j.scs.2022.103953, 2022.

705